Application of a three-dimensional unstructured-mesh finite-element flooding model and comparison with two-dimensional approaches

T. Zhang[a,b], F. Fang[b,*], C. C. Pain[b], Č. Maksimović[c], P. Feng[a], I. M. Navon[d,b], P. D. Bates[e]

[a] *State Key Laboratory of Hydraulic Engineering Simulation and Safety,Tianjin University, Tianjin 300072, China*
[b] *Applied Modelling and Computation Group, Department of Earth Science and Engineering, Imperial College London*
[c] *Civil and Environmental Engineering Department, Imperial College of London, Technology and Medicine, Imperial College Road, SW7 2BU, London, UK*
[d] *Department of Scientific Computing, Florida State University,Tallahassee, FL, 32306-4120, USA*
[e] *School of Geographical Sciences, University of Bristol, Bristol, BS8 1SS, UK*

Abstract

Urban flood modelling plays a key role in assessment of flood risk in urban areas by providing detailed information of the flooding process (*e.g.* location, depth and velocity of flooding). Accurate modelling results are the basis of reliable flood risk evaluation. In this paper, a new 3D unstructured mesh urban flooding model developed in [1] has been applied to a flood event in a densely urbanized area within the city of Glasgow. Good agreement has been achieved when comparing the results with those published in other 2D shallow water models [2, 3] in ponded areas. However, larger vertical velocity ($> 0.2\,m/s$) and larger differences between the 3D and 2D model can be observed in areas with greater topographic gradients ($> 3\%$). Through the modelling of a real flooding event this paper helps illustrate the case that 3D modelling techniques are promising to improve accuracy and obtain more detailed information related to urban flooding dynamics. This helps to obtain better assessments of flood damage and vulnerability of urban areas. To the

*Corresponding author
Email address: f.fang@imperial.ac.uk (F. Fang)

best of our knowledge, this is the first paper to apply a 3D unstructured mesh finite-element model to a real urban flooding event. It highlights some of the differences between the 3D and 2D urban flood modelling results.

Keywords: Three-dimensional modelling, Urban flooding, Finite element method, Unstructured mesh, Vertical inertia.

1. Introduction

Over the last half century, the worldwide rapid increase in urbanization has caused a drastic change of land use [4]. The increase in impervious surfaces (*e.g.* roofs, roads, etc.), all kinds of other hardened surfaces and compaction of soils [5] enhances the risk of urban flooding [6, 7]. Flooding in urban areas is also more hazardous due to a high concentration of inhabitants and economic actors [8] and the overland flow on relatively smooth impermeable surfaces [4]. Due to this, demand for flood risk management and hazard loss reduction in urban areas has increased, and a wide variety of modelling tools have been proposed.

Since the mid 1960s, computer models have been used to simulate the behaviour of urban flooding [10]. In recent years, researchers have focused on questions such as the treatment of wetting and drying [11], trade-offs between accuracy and computational efficiency [12, 13, 14], friction parameterization [12], the application of new computational techniques and new data sources [15, 13], as well as reduced complexity models [16].

With the availability of high-quality topographical data and the increase of computational power there is now an increased emphasis on developing highly accurate modelling techniques for flood inundation ([17, 18, 19]). Humberto *et al.* [13] have used an unstructured grid, Godunov-type, finite volume model to simulate a dam-break flooding event in an urban residential area, and validated their model with high-resolution data. Brown *et al.* [20] have adopted a coupled storm surge and overland flow model, which is based on a shock-capturing numerical scheme and high-resolution topographic data, to simulate extreme flooding in an urban area.

The trade-offs between modelling accuracy and computational efficiency certainly merit consideration. Fewtrell et.al [14] have evaluated the effectiveness of coarse grids to represent flooding through urban environments by applying a 2D storage cell model, LISFLOOD-FP, and pointed out that, critical length scales related to building dimensions and building separation distances deter-

mine the coarsest useful grid resolutions. Julien [8] has introduced a source term to represent the head losses due to singularities of the topography in urban areas (*e.g.* at the corners of buildings) based on the method of porosity to account for the reduction in storage and the exchange sections. Qiuhua Liang et.al [21] have applied an adaptive quadtree grid-based shallow water equations solver which dynamically adapted the grid to represent the critical flow features such as steep water surface gradients and wetting-drying fronts. This method has proved to be able to improve computational efficiency of two-dimensional numerical models for large-scale flood simulation. Meanwhile, some other researchers have proposed that hydraulic modelling needs to use reduced complexity approaches for rapid solutions. With regards to these simple spatially-distributed models, Hunter and Bates have carried out a review elaborating the theoretical basis and summarizing the recent progress [22].

Most of the extensive literature on urban flooding uses either 2D models [21, 2] or 1D/2D coupled models [3] in order to obtain high speed modelling. However, urban flood flows have three-dimensional (3D) characteristics. This is because, in urban areas, buildings behave as obstacles, leading to hydrodynamic forces like stagnation pressure, lateral shear and flow separation [23]. Lane *et.al* [24] found that 3D computational fluid dynamics (CFD) models provide more reliable estimates of bed shear stress. They provide more information of the 3D flow structures, and better representation of the flow process than 2D models. Therefore three-dimensional models in combination with higher-quality of datasets are required in order to improve our understanding of urban flooding. Recent research carried out by Galambos *et.al* [25, 26] provided innovations in analyzing important local conditions of interfacing surface run-off and underground pipe network through the inlet structure (gully) revealing a number of issues which cannot be analyzed by standard 2D models.

In this work, a newly developed 3D urban flooding model[1] has been applied to a flooding event in a densely urbanized area within the city of Glasgow. Its performance has been assessed by comparing 3D model results against those obtained from 2D models where high-quality topographic data is used. The advantages of 3D urban flooding are demonstrated in this complex urban area. This is the first time that this kind of evaluation of 3D models has been performed for realistic urban flood modelling.

The structure of the present paper is as follows. The next section outlines the proposed 3D unstructured-mesh flooding model. In section 3, the model is

applied to a flooding event in Glasgow, Scotland, United Kingdom, which has previously been modelled with six different 2D models (TUFLOW, DIVAST, DIVAST-TVD, TRENT, JFLOW, LISFLOOD-FP) in [2]. A comparison with these 2D models and an assessment of the 3D model is also provided. In the final section conclusions are drawn.

2. 3D Navier-Stokes model methodology

In this section, the governing equations and boundary conditions are introduced in the domain of interest $\Omega \subset \mathbb{R}^3$ and its boundary Γ. For free-surface flow problems, the boundary Γ is split into the free-surface boundary Γ_s and the rest $\Gamma_b = \Gamma - \Gamma_s$, and the domain is vertically variable with time due to the surface movement. When wetting and drying occurs, the horizontal extent of Ω is then time-dependent.

2.1. Governing equations

The underlying equations are the incompressible Navier-Stokes (N-S) equations in a time-dependent domain Ω:

$$\nabla \cdot \vec{u} = 0, \tag{1}$$

$$\rho(\frac{\partial \vec{u}}{\partial t} + \vec{u} \cdot \nabla \vec{u}) - \nabla \cdot (\mu + \mu_\tau)\nabla \vec{u} + \nabla \overline{p} = -\rho g \vec{k}, \tag{2}$$

where $\vec{u} = (u, v, w)^T : \Omega \times [0, T) \rightarrow \mathbb{R}^3$ is the velocity for the considered time interval [0, T), $p \in \Omega \times [0, T)$ is the pressure, $-\vec{k}$ and g are the gravity direction and magnitude respectively, ρ the density, and μ the fluid dynamic viscosity and μ_τ is the sub-grid scale (SGS) viscosity which for simplicity, is specified as a constant and chosen to filter out the small scale unresolvable turbulent features based on a cell Reynolds number of 2. Note that the cell Reynolds number exceeding 2 may lead to oscillation of numerical solutions [42].

2.2. Boundary conditions

2.2.1. No-normal flow boundary condition

For the time being, no water exchange through the bottom of the domain Γ_{bottom} (infiltration or superflux) has yet been taken into account, therefore,

no-normal flow boundary condition is unusually enforced on the bottom of the domain:

$$\vec{u} \cdot \vec{n} = 0 \;\; on\, \Gamma_{bottom} \tag{3}$$

With this boundary condition, fluid can only flow along the boundary, but not through it. Similarly, if the sides of the computational domain have no water exchange, no-normal flow boundary condition apply as well.

2.2.2. Combined kinematic free-surface boundary condition with wetting and drying

The free-surface of the domain moves along with the change of the water height, as well as the wetting and drying process. A combined kinematic free-surface boundary condition is adopted on the free-surface in wet areas, while a no-normal flow boundary condition is enforced on the free surface in dry areas (see figure 1). The free-surface kinematic boundary conditions are

$$\vec{n} \cdot \vec{k} \frac{\partial \eta}{\partial t} = \vec{n} \cdot \vec{u}, \tag{4}$$

where, $\vec{n}$ is the unit normal to the free surface, $\vec{k}$ is a general upward unit normal (usually for simplicity the upwards direction is assumed to be in the z direction, *i.e.* $\vec{k} = (0, 0, 1)$). Detailed derivations of the equation above can be found in [11].

When wetting and drying happens, the free-surface might fall below the ground surface, *i.e.* in dry areas, which will lead to a invalid domain. Therefore, a positive water level/water depth has to be ensured, and the free-surface height η must be constrained so as not to fall below the threshold value d_0 off the bottom (see figure 1), *i.e.*

$$\eta = max\{\frac{p}{\rho g},\;\; -H_b + d_0\};\;\; d = max\{\frac{p}{\rho g} + H_b,\;\; d_0\}, \tag{5}$$

where the pressure p in the domain is relative to that at the datum surface, H_b is the elevation of the bottom relative to the datum surface, d is the water depth and $d_0 \in R$ is a threshold constant which defines the minimum allowed water depth.

Taking into account $p = \rho g \eta$ and ensuring a positive water level $\eta = max(\frac{p}{\rho_0 g}, -H_b + d_0)$ on the free surface Γ_s, yields the combining kinematic free surface bound-

ary condition:

$$\vec{n} \cdot \vec{k} \frac{1}{\rho g} \frac{\partial}{\partial t} max(p, \rho_0 g(-H_b + d_0)) = \vec{n} \cdot \vec{u}, \tag{6}$$

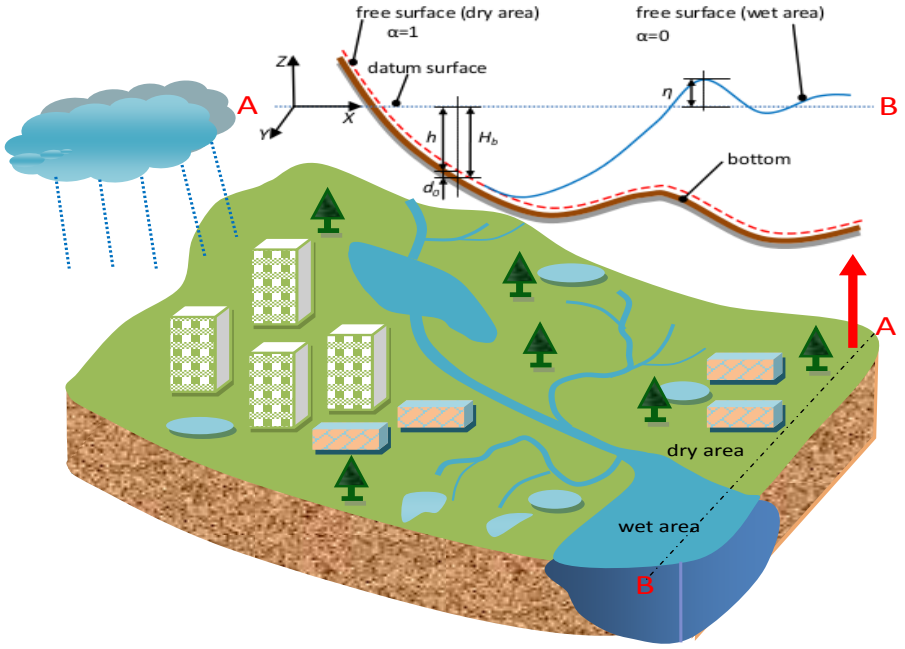

Figure 1: Schematic of an idealized domain geometry, featuring a wet area and a dry area (thin film).

The boundary conditions described above can be used to solve the governing equations (N-S equations) and obtain the pressure thus the free-surface height. A variable α is introduced to represent the wet/dry interface. The value of α is calculated by:

$$\begin{aligned}
&\alpha = 0 \text{ if } \ d > d_{min}, \ \text{ wet areas;} \\
&\alpha = \frac{d_{min} - d}{d_{min} - d_0} \text{ if } d \in [d_0, d_{min}], \ \text{ transient areas;} \\
&\alpha = 1 \text{ if } d < d_0, \ \text{ dry areas.}
\end{aligned} \tag{7}$$

In wet areas of the domain $\alpha = 0$, $p \geq \rho_0 g(H_b + d_{min})$. In dry areas $\alpha = 1$, $p < \rho_0 g(H_b + d_0)$, but the free-surface elevation η is set to a constant value $H_b + d_0$, *i.e.* the free-surface elevation η is seperated from pressure p and the no-normal flow boundary condition is fully switched on, in this case. A relaxation of this boundary condition is used when $d \in [d_0, d_{min}]$.

2.2.3. Bottom drag force

On the bottom surface of the computational domain, there is a bed drag force imposed by the ground surface due to its roughness. A commonly used bottom stress parametrization is the Manning-Strickler formulation:

$$\vec{n} \cdot \mu \nabla \vec{u} = n_m^2 g \frac{|\vec{u}|\,\vec{u}}{d^{1/3}}, \quad \text{on}\, \Gamma_{bottom}, \tag{8}$$

where n_m is the Manning coefficient.
As a d_0 thin layer is enforced in the whole domain, this causes non-physical flow in dry areas. In order to prevent the non-physical flow, the Manning-Strickler coefficient in dry areas should be set to a large value:

$$n_m|_{\Gamma_{dry}} = n_m + max(0, \frac{d_{min} - d}{d_0} \times n'_m), \quad d_0 \leq d \leq d_{min}. \tag{9}$$

Here, n'_m is a relatively large number, for example 10^3.

2.3. Conditioning of the equations in high aspect ratio

In finite element methods, both the continuity equation and momentum equation need to be discretized spacially and temporally. Integrate the discretized form of the continuity equation and momentum equation in the computational domain, one can obtain:

$$\int_\Omega M_i \nabla \cdot \vec{u}^{n+1} d\Omega = 0, \tag{10}$$

$$\begin{aligned} \int_\Omega N_i \rho \frac{\vec{u}^{n+1} - \vec{u}^n}{\Delta t} d\Omega \;\; &= \;\; \int_\Omega N_i \{ -\rho \vec{u}^{n+1} \cdot \nabla \vec{u}^{n+1} + \nabla \cdot \mu \nabla \vec{u}^{n+1} \\ &\quad -\nabla p^{n+1} - \rho g \vec{k} \} d\Omega \end{aligned} \tag{11}$$

where $\vec{n}$ denotes the unit normal vector to Γ, N_i and M_i are the basis functions of velocity and pressure respectively. Introduce an absorption (σ) term into the momentum equation (the detailed derivations can be found in [1]):

$$\int_\Omega N_i \rho \frac{\vec{u}^{n+1} - \vec{u}^n}{\Delta t} d\Omega = \int_\Omega N_i \{ -\rho \vec{u}^{n+1} \cdot \nabla \vec{u}^{n+1} + \nabla \cdot \mu \nabla \vec{u}^{n+1} - \nabla p^{n+1} - \sigma(\vec{u}^{n+1} - \vec{u}_*^{n+1}) - \rho_*^{n+1} g \vec{k} \} d\Omega, \quad (12)$$

where $\vec{u}_*^{n+1}$, ρ_*^{n+1} are approximations to $\vec{u}^{n+1}$, ρ^{n+1} and calculated from the pressure at the previous time level or the previous iteration at the current time level, Δt is the computational time step size, n is the time level and the inverse time scale for the vertical velocity relaxation is:

$$\sigma = \begin{pmatrix} 0 & 0 & 0 \\ 0 & 0 & 0 \\ 0 & 0 & \sigma_{zz} \end{pmatrix}, \quad (13)$$

with

$$\sigma_{zz} = \frac{(\Delta x)^2}{\Delta t a^2 (\Delta z)^2}, \quad (14)$$

in high aspect ratio domains, where $\Delta x, \Delta z$ are the finite element length scales in the horizontal and vertical respectively, a is the tolerable aspect ratio of the element length scales.

3. Model application

The proposed 3D urban flood inundation model is applied to a $1.0\,km \times 0.4\,km$ densely urbanized area within the city of Glasgow, Scotland, UK (see figure 2) where a flood event occurred on 30^{th} July, 2002. The flood was triggered by the surcharged flow from a culvert which drains upstream catchment run-off. Water enters the study domain from the north-east corner and quickly spreads west and south along the streets and roads before ponding on low-lying areas in the southern part of the domain. The terrain data of this case is generated using a combination of airborne laser altimeter (LiDAR) fused with digital map data with $2\,m$ resolution (details about the generation process of the map can be found in [2]). Buildings are represented as blocks through raising the elevation by either $12m$ or $6m$ to represent building height, respectively. This is referred to as the *building-block* method in [3].

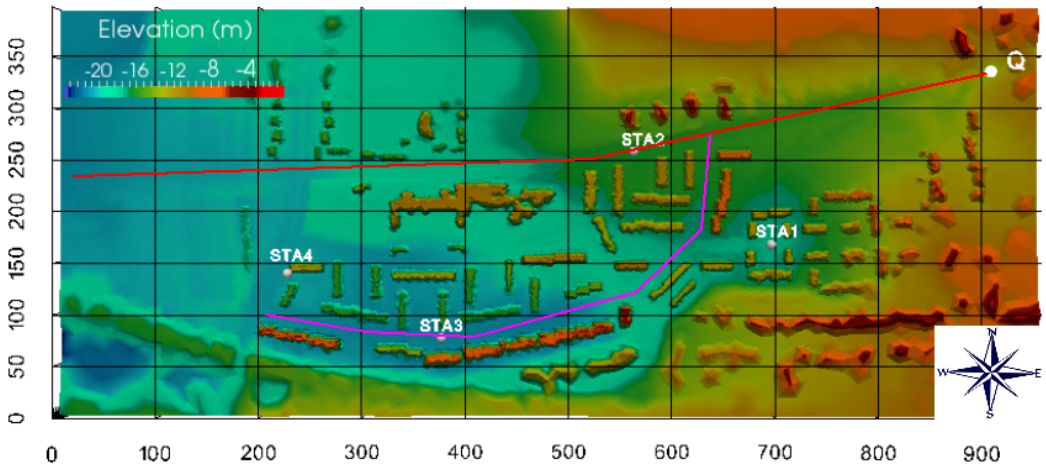

Figure 2: Topography of the study area and the locations of flooding source and detectors (same locations as in [3]), dimensions in m. The red line marks the main east-west street, while the magenta line shows crescent street.

The unstructured meshes are initially created as 2D (triangle elements) by Gmsh [28], and then extruded downwards (in the direction of gravity) to layered 3D (tetrahedral elements) by Fluidity [29] on which simulations can be performed (see figure 3). In order to examine the sensitivity of flood simulation to mesh resolution, three different 3D unstructured tetrahedral meshes with element lengths of $2\,m$, $5\,m$, $10\,m$ in horizontal have been used for the modelling (see figure 4), while the vertical element lengths are determined by the water depth. At the beginning of the simulation, the whole domain is dry and the vertical element length is d_0 (very small) everywhere. As the water flows into the domain, some parts become wet and the water depth increases. Thus the element length in vertical changes accordingly in these wet areas but stays the same (d_0) in the dry areas. Table 1 lists the properties of these meshes used in the Glasgow case, where the meshes with the resolution of $5\,m$ and $10\,m$ are uniformly unstructured, while the fine ($2\,m$) mesh is multi-scale unstructured, *i.e.* the high ($2\,m$) resolution is used in the areas along the flood pathway while the lower resolution in less important regions (see figure 5). By using the multi-scale mesh, the computational expense can be reduced while the accuracy of modelling is comparable with an uniform $2\,m$ mesh.

This flooding event is mainly caused by a flow out of a culvert (located at the point labelled Q in figure 2). The inflow boundary condition is determined

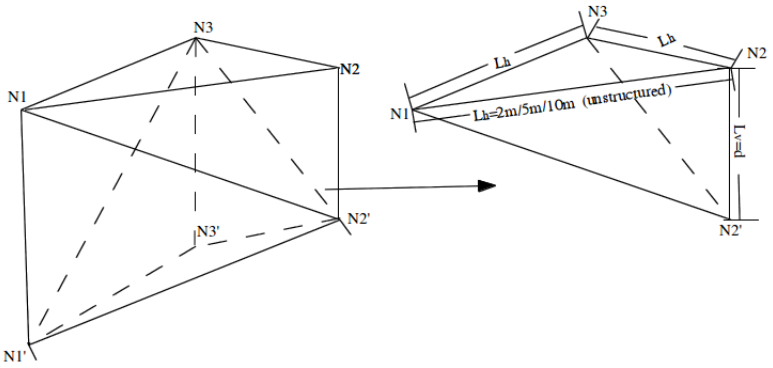

Figure 3: $N1N2N3$ is a triangle element of a 2D mesh created by Gmsh. Fluidity extrudes the 2D mesh downwards to 3D, in which the lengths of $N1N1'$, $N2N2'$ and $N3N3'$ are equal to the water depth at these three locations. Nodes $N1-3$ are on the top surface of the domain which is always flat and horizontal, and $N1'-3'$ are on the bottom surface which is determined by the topography. The prismatic volume $N1N2N3N1'N2'N3'$ is divided into three tetrahedral elements $N1N2N3N2'$, $N1'N2'N3'N3$ and $N1N3N1'N2'$ (left). On the right is one of the tetrahedral elements of the 3D mesh, where L_h and L_v are the horizontal and vertical element lengths respectively. L_h is specified in Gmesh as $2m/5m/10m$ (unstructured), and L_v is equal to the water depth d (d_0 in dry areas, see equation 5).

Element length in horizontal	$2\,m$	$5\,m$	$10\,m$
Number of cells	170586	126708	33228
Number of nodes	57016	42794	11362

Table 1: The number of tetrahedral elements and nodes of the unstructured meshes used in the 3D Glasgow modelling.

from a hydrograph/discharge profile (see figure 6) which determines the velocity normal to the circle shown at Q. Since no monitoring was performed during the flood, this hydrograph was assessed from [2] and reflected their best interpretation of available historical photography. The surcharged flow from the culvert started running at $t = 5\,min$ from the beginning of the numerical experiment and reached its peak between 22 and 24 min and ended at $t = 40\,min$. No-normal-flow boundary condition are enforced at all the external boundaries and at the bottom of the domain. A Manning roughness coefficient $n_m = 0.015\,m^{-1/3}s^{-1}$ is assigned to all roads and $n_m = 0.05\,m^{-1/3}s^{-1}$ is used everywhere else, as described in [2]. A thin layer of water has been assumed everywhere to account for the wetting and drying process, and the

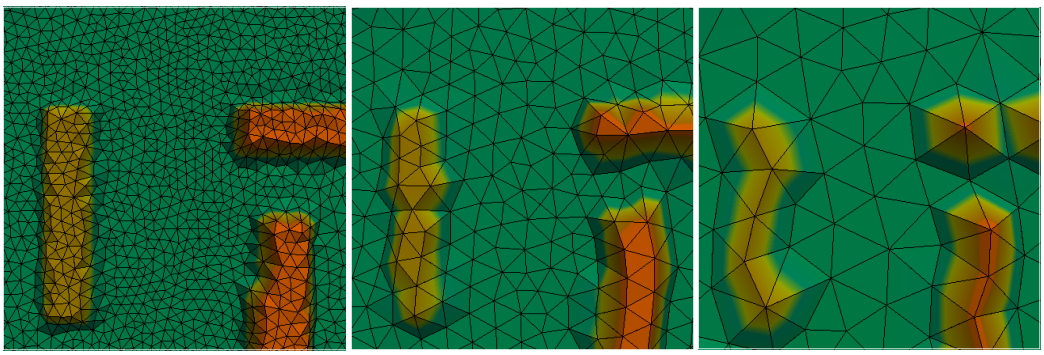

$\Delta x = 2\,m$ $\Delta x = 5\,m$ $\Delta x = 10\,m$

Figure 4: Zoom-in plain view of different meshes used in the 3D model.

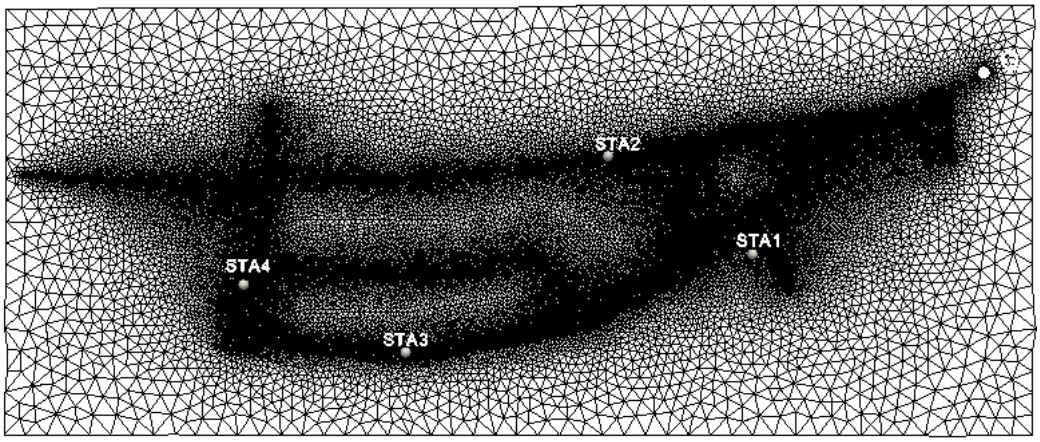

Figure 5: Multi-scale mesh with $2\,m$ resolution along the key flood pathways (plain view). $STA1-4$ are four locations selected for local flow study.

thickness in dry areas is set to $d_0 = 0.01\,m$ (much less than the LiDAR data vertical error of $5\,cm$ [40, 41]). The implicit, in time, and discretized, in space, three-dimensional Navier-Stokes equations (both continuity and momentum equations) are solved with a fixed time step of $\Delta t = 1s$ in all the simulations performed in this paper (although large time step can be used in the implicit 3D model, we used $1s$ in order to ensure the accuracy of results). To avoid non-physical and/or diverge solutions, an eddy viscosity tensor field $(1, 1, 0.1)m^2/s$ is specified for turbulent flows in the domain based on the cell Reynolds number of 2. Continuous piecewise linear functions are used for

both velocity and pressure spacial discretisation. The analysis based on this case will focus on four parts: (1) the 3D representation of the flow and flooding inundation (velocity and water depth); (2) the effect of 3D modelling in urban flood simulation; (3) the comparison between the results from the proposed 3D model and results from other commonly used 2D models; and (4) the effect of mesh resolutions on the results.

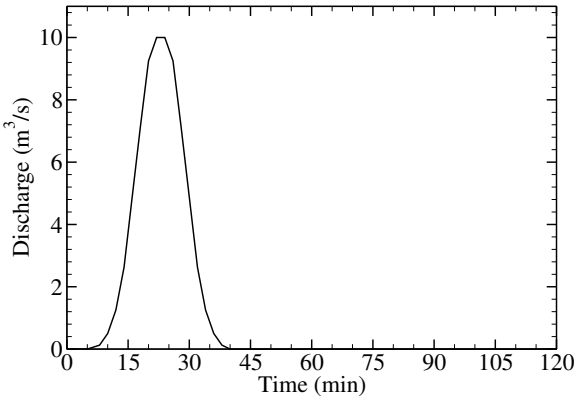

Figure 6: Discharge profile at location labelled Q in Fig.2 which is obtained from observations of the July, 2002 flooding event.

3.1. Flood inundation

Figures 7-8 show the velocity magnitude and water depth at time levels $t = 20, 30, 40, 60\,min$ respectively. These 3D modelling results show the different development stages of the flooding between 5 and $40\,min$ (during this period, water flows into the domain and reaches a maximum inflow discharge of $10\,m^3/s$ at $t = 22 - 24\,min$), as well as the flood inundation and recession processes after $t = 40\,min$ (inflow ends at $t = 40\,min$ as mentioned before). It can be observed that the water wave propagates westwards along the main road and flows into the adjacent streets and lanes. At time level $t = 20\,min$, the flood reaches the intersection of the main east-west street and the crescent street (see figure 2), and divides into two branches (note: some of very small pools shown in the figures are due to the unphysical flow in the thin layer in the dry areas). It can be seen that the water depth in most of the inundated area is greater than $0.2\,m$ at $t = 20\,min$ while the maximum water depth is $1.56\,m$ (see figures 8(a)) at around the source point Q. The largest velocity reaches $3.78\,m/s$ at a steep slope close to the source

(see figures 7(a)). The vertical velocity component ranges from $-0.58\,m/s$ to $-0.12\,m/s$ and becomes large ($> 0.2\,m/s$) on relatively steep slops ($> 3\%$) (see areas marked with a rectangle and a square in figures 7(a) and 9(a)).
The flood continues to propagate westward and terminates at around location $(150, 250)\,m$ (see figure 2) which is consistent with prediction from the 2D diffusion wave models (JFLOW and LISFLOOD-FP (versions before 2008)) [2]. By the time level $t = 30\,min$, the flood inundation has reached $STA3$ and $STA4$. The vertical velocity at its maximum is $-0.66\,m/s$ along a downward direction at the first slope along the pathway around $STA1$ (the area marked with a square in figure 7(a)).
During the period $t = 40 - 60\,min$, the flood gradually recedes from the main road in the northern part of the domain. The water accumulates in the low-lying area in the south-west, and ponds in depressions, particularly in the vicinity of $STA3$ and $STA1$ (figures 8(c) and 8(d)) where the maximum water depth rises to $1.93\,m$.

3.2. Effect of 3D modelling in urban flooding simulations

As discussed above, flood inundation scenarios predicted from 3D modelling are mostly in agreement with those from 2D models in [2]. However, compared with 2D modelling, 3D modelling can provide better information about the local flow structures where vertical inertia is important. This can be observed from spatial distribution of velocity and its vertical component (see figures 7 and 9). It is found that large vertical velocities ($> 0.2\,m/s$) often appear around the edges of buildings or on relatively steep slopes ($> 3\%$) where topographic contour lines are relatively close. The maximum velocity reaches as high as $4.05\,m/s$ at $t = 25\,min$, while the maximum vertical velocity reaches $0.34\,m/s$ (with a depth of $1.4\,m$) at $t = 32\,min$ along the upward direction and $0.72\,m/s$ (with a depth of $0.12\,m$) at $t = 25\,min$ along the downward direction during $t = [25, 40]\,min$ when the flood spreads across most of densely urbanized areas. The maximum water depth at the lowest-lying area (around location STA3) reaches $1.9\,m$ at time level $t = 60\,min$. Figure 10 depicts the time series of the maximum vertical velocity component.
As seen in the numerical modelling results, the vertical component of velocity is appreciable and can not be omitted for the sake of accuracy. Since depth-damage curve estimation is the most commonly used method in urban flood damage assessment [31], it seems that 2D models are good enough if they can predict similar extents and depths as 3D models. However, the force and

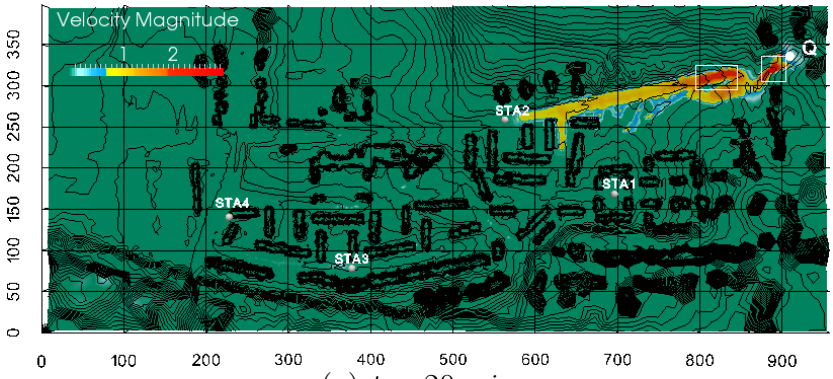

(a) $t = 20\,min$

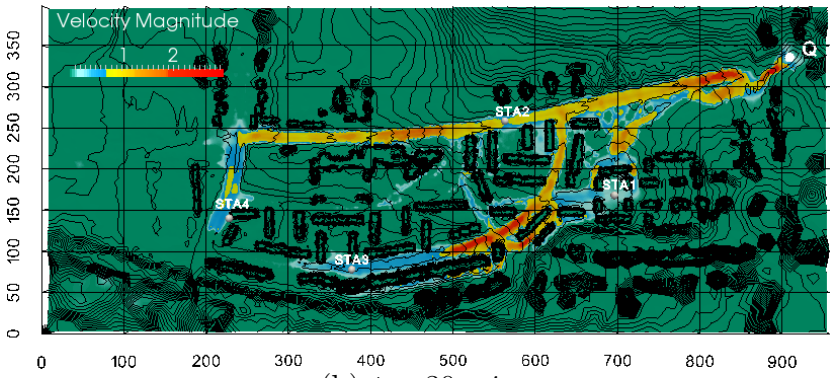

(b) $t = 30\,min$

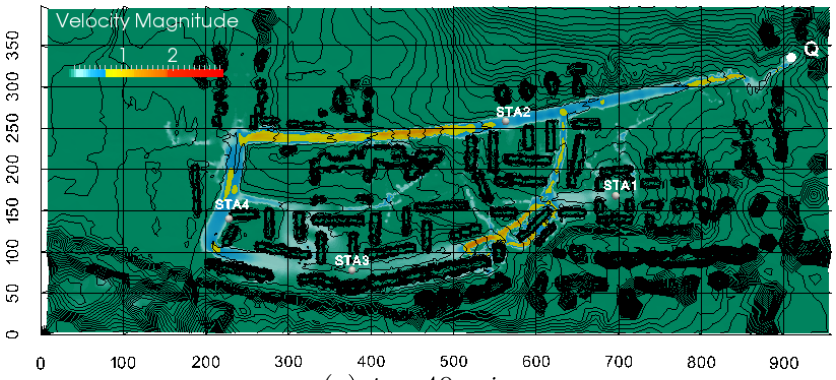

(c) $t = 40\,min$

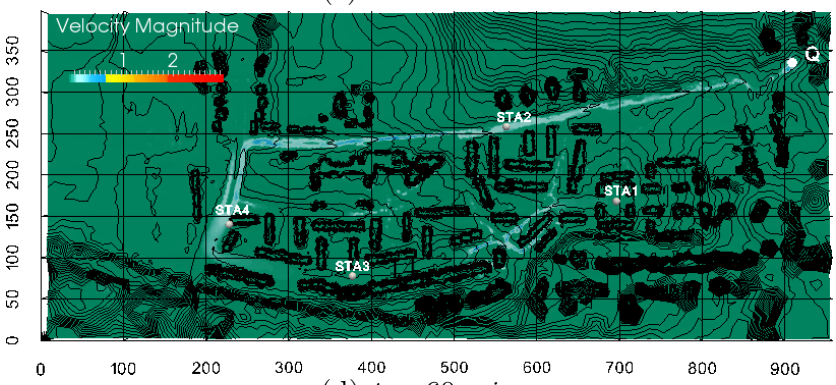

(d) $t = 60\,min$

Figure 7: Velocity magnitude at time level $t = 20,\ 30,\ 40,\ 60\,min$, and contours representing the topographic gradient, where denser contours denote steeper slope.

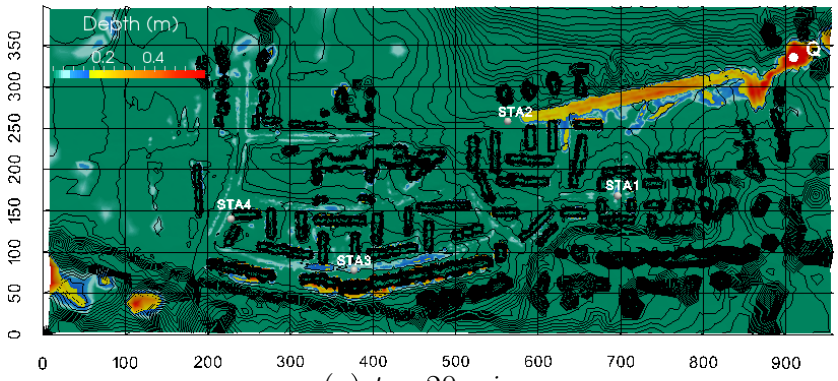

(a) $t = 20\,min$

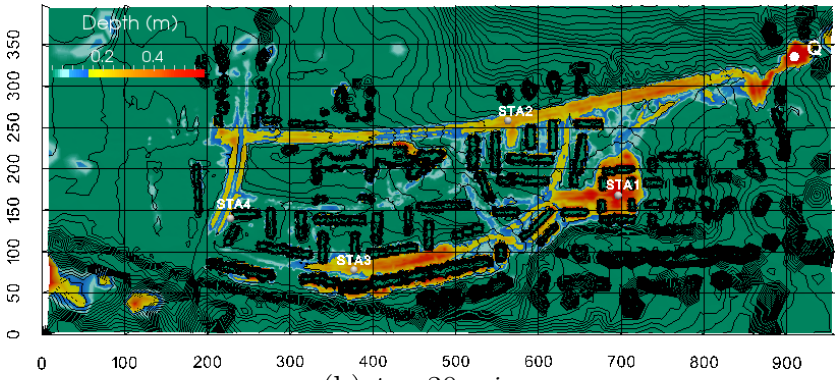

(b) $t = 30\,min$

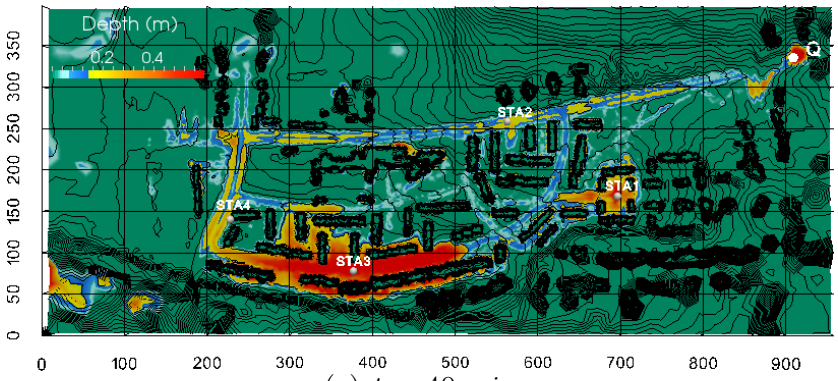

(c) $t = 40\,min$

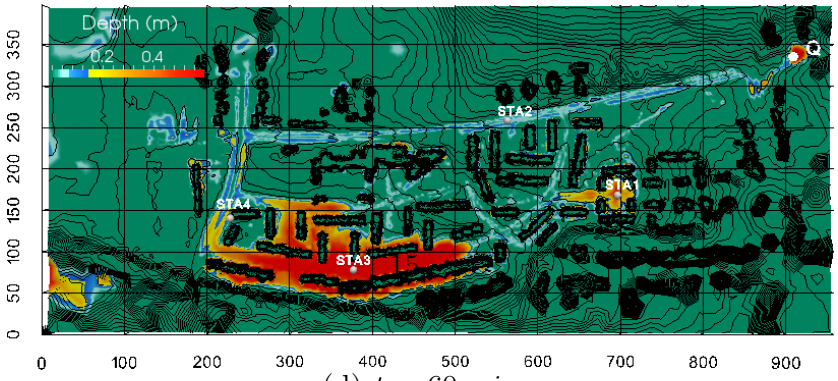

(d) $t = 60\,min$

Figure 8: Water depth at time level $t = 20,\ 30,\ 40,\ 60\,min$.

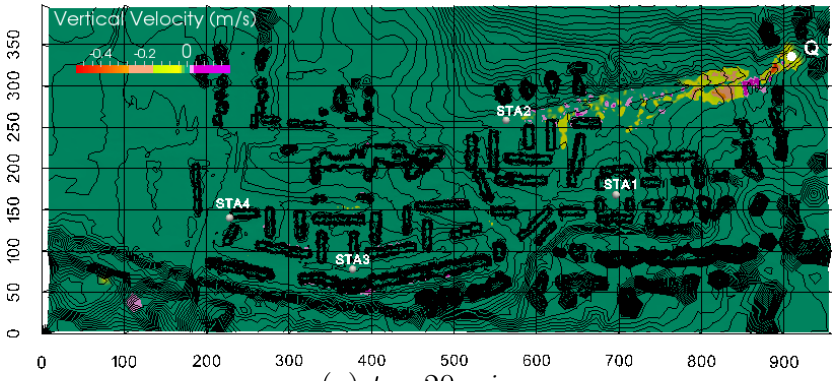

(a) $t = 20\,min$

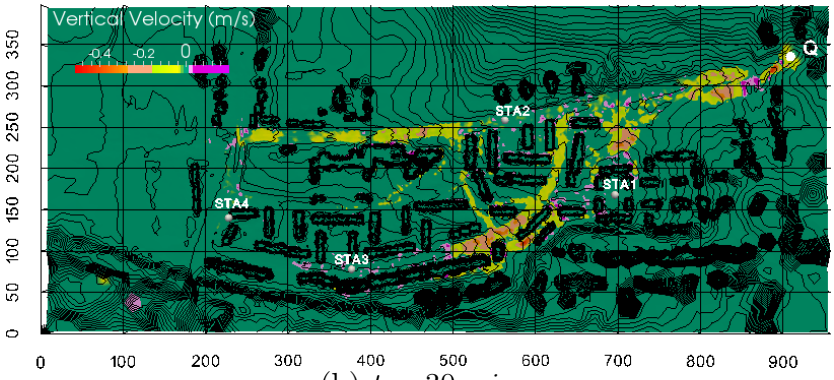

(b) $t = 30\,min$

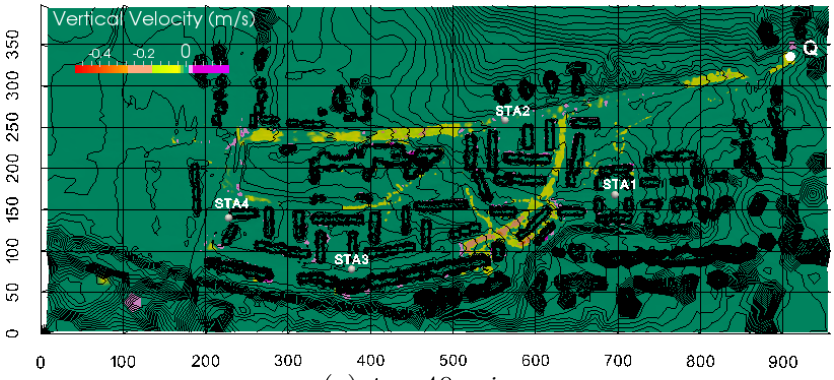

(c) $t = 40\,min$

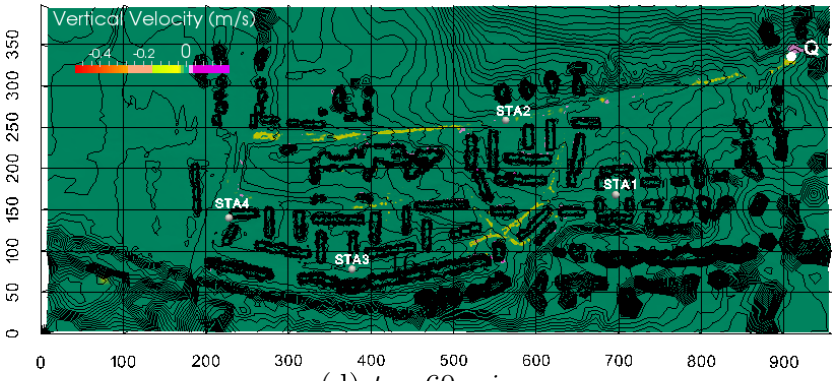

(d) $t = 60\,min$

Figure 9: Vertical velocity at time level $t = 20,\ 30,\ 40,\ 60\,min$.

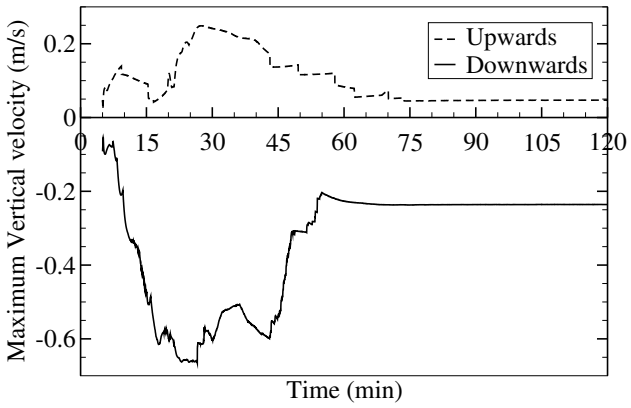

Figure 10: Time series of maximum vertical velocity component over the computational domain.

velocity of flood water, which are usually neglected in 2D models, have also been recognized as important factors which need to be taken into account in risk assessment models, especially for floods caused by defence failures and urban storms [32], and 3D models are able to provide more detailed information about these factors. Smith [33] has pointed out that a combination of velocity and depth of floodwaters is needed to evaluate the structural damage if subjected to the combination of deep and high velocity flood water. With the analysis of the 3D results above, we believe, although not included in this work, that the 3D modelling technique opens interesting perspectives in risk assessment. It could enable building failure to be determined from the forces exerted by the flows on the buildings. 3D simulation, in addition to providing confirmation, or otherwise, of the accuracy and robustness of 2D modelling in urban flood research, can provide additional information on the flow structure in cases where the vertical velocity plays an important role.

3.3. Enlarged 3D section views

The figures above are plain views of the whole domain which show the flood propagation process from a macro perspective. For 3D modelling, one may be also interested in the local flow characteristics, as 3D models are expected to give more detailed and direct information about local flows. In this subsection, the local flows around $STA1$, $STA2$ and $STA3$ (locations see figure 5) are presented. In order to look into the details of the local flows, firstly the whole domain is clipped and the cross-sections which pass through the three locations are generated (see figure 11). In this way, the local flow details can

be seen clearly around each location with the vertical expanded by a factor of 10. Figures 12-14 show the enlarged views of the cross section around the locations. Note that in order to show the local flows, these images have been rotated by a certain angle (see the direction of the compass in figures 12-14).

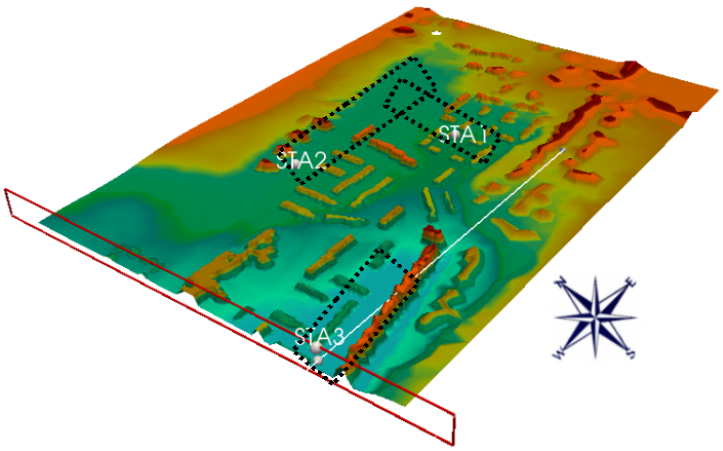

Figure 11: Section clip at $STA3$, where the local flows in the areas marked with the black dash-line boxes will be shown in figures 12-14.

Figure 12 shows the local flow details around $STA1$. The flood water comes from the north, flows around the buildings, reaches the low-lying area round $STA1$ and ponds there. Strong local currents (dense arrows in figure 12) and large vertical velocities can be observed around the edges of buildings and on relatively steep slopes. The flow velocity reaches its maximum at $t = 23min$ (see figure 12(b)), then gradually decreases with the increase of the water depth (see figure 12(c)-(d)).
The progression of water passing $STA2$ is shown in figure 13. The water at $STA2$ comes from the east along the main street. Different from the area around $STA1$, the water depth keeps relatively small and velocity keeps relatively large at this location. This is because this location is on a slope (see figure 2), so it has better conditions for flowing rather than ponding. The flow characteristics in the vicinity of $STA4$ are similar to that in the vicinity of $STA2$.
Figure 14 shows the details of local flows around $STA3$. The flood water arrives at $STA3$ around $t = 30\,min$. After $t = 40\,min$, the water ponds in the vicinity of $STA3$ (see the change of the mesh in figure14(c)-(d)) and the water depth reaches its maximum at $t = 60\,min$ since this is the lowest-lying

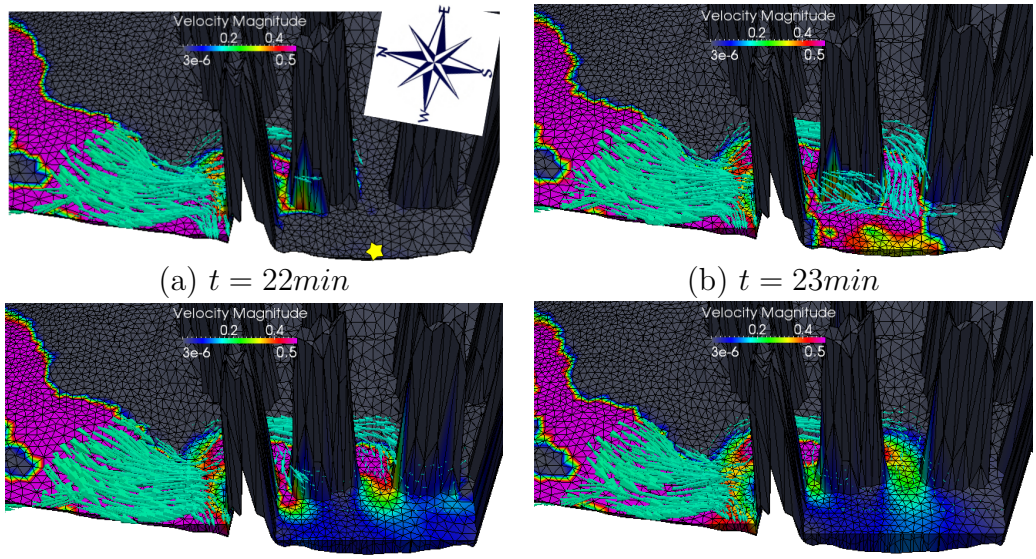

(a) $t = 22min$ (b) $t = 23min$

(c) $t = 25min$ (d) $t = 30min$

Figure 12: Enlarged vertical section view shows the local flow details around $STA1$ (the yellow star in (a)), in which the colour map and vectors represent the velocity magnitude and direction respectively, and the mesh movements in the vertical represent the change of water depth.

area.

3.4. Sensitivity of the proposed 3D model to mesh resolution

Figure 15 shows flood extents predicted using different mesh resolutions ($2\,m$, $5\,m$, $10\,m$). This figure presents areas of model agreement (match) and areas where flooding is only predicted by one of these three meshes. We can see more lateral inundation using $2\,m$ mesh resolution while more westerly inundation using $10\,m$ mesh resolution. The inundation extent of $5\,m$ mesh modelling prediction is very close to that predicted by using $2\,m$ mesh resolution. This pattern of the flood extent varying with mesh resolution of the 3D results is quite different from the 2D results in [3], where finer mesh predicts greater flood extent westwards and a slightly smaller extent in the north-south direction. A likely explanation for this is that the vertical inertia has an appreciable effect on sensitivity of the flooding model to mesh resolution. The decrease in lateral spreading and increase in the longitudinal propagation of the coarser mesh, may be due to flow truncation errors or

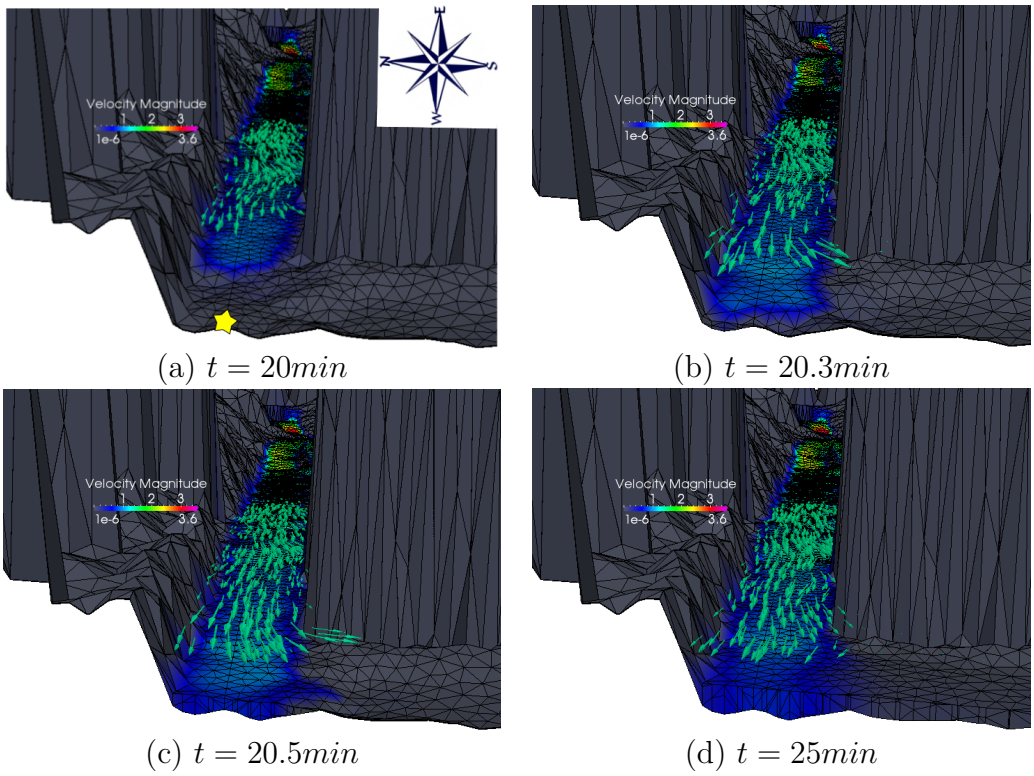

(a) $t = 20min$ (b) $t = 20.3min$

(c) $t = 20.5min$ (d) $t = 25min$

Figure 13: Enlarged vertical section view shows the local flow details around $STA2$ (the yellow star in (a)), in which the colour map and vectors represent the velocity magnitude and direction respectively, and the mesh movements in the vertical represent the change of water depth.

numerical diffusion [34].

Figure 16 shows water depth at $STA1 - 4$ of the 3D flooding model and BREZO-BB 2D model from [3] respectively using three different meshes. Although the 3D results from the $10\,m$ mesh resolution and 2D results from $0.8\,m$ mesh resolution cannot be compared, the former is useful for demonstrating the ability of the 3D model using a coarse mesh, and the latter can be used as a reference solution in [3]. It can be observed that the effect of coarsening the mesh is similar for both of the 3D and 2D BREZO-BB models. In both models, the finer mesh predicts deeper water at $STA2$ but shallower water at $STA3$ and $STA4$. Compared with the 2D BREZO-BB model, the 3D model provides better predictions when using coarser meshes.

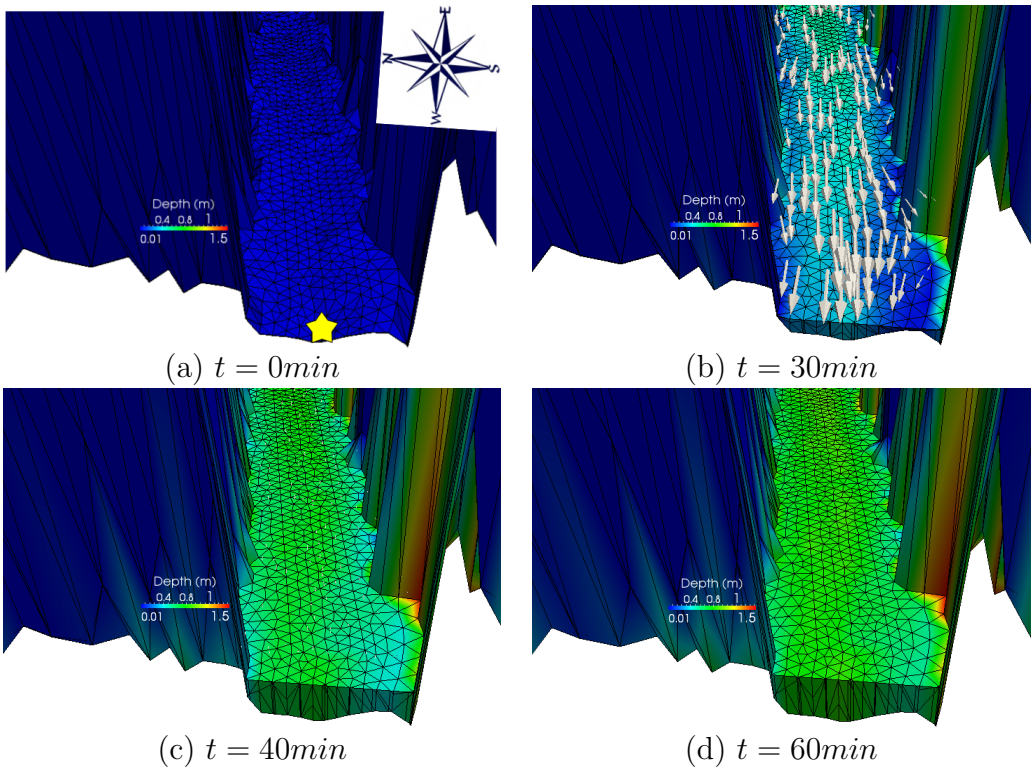

Figure 14: Enlarged vertical section view shows the local flow details around $STA3$ (the yellow star in (a)), in which the colour map represents the water depth, the vectors represent the velocity direction, and the mesh movements in the vertical represent the change of water depth.

Specifically, with the $5\,m$ mesh, the 3D model is able to give predictions very close to the $2\,m$ mesh result at all the detectors, while the predictions of 2D BREZO-BB model are quite different from those using finer meshes ($2\,m$ and $0.8\,m$). Even with $10\,m$ mesh resolution, the 3D model is capable of providing more reasonable results than the 2D BREZO-BB model using $5\,m$ mesh resolution. When the mesh is coarsened to $10\,m$ in the 3D model and $5\,m$ in the 2D BREZO-BB model, it is seen that ponding deeper than $0.3\,m$ appears at $STA4$.

3.5. Sensitivity analysis of model responses to the inflow discharge

This section aims to examine the effect of the uncertainty in the inflow discharge on model solutions, *e.g.* water depth and velocity. The 3D N-S model

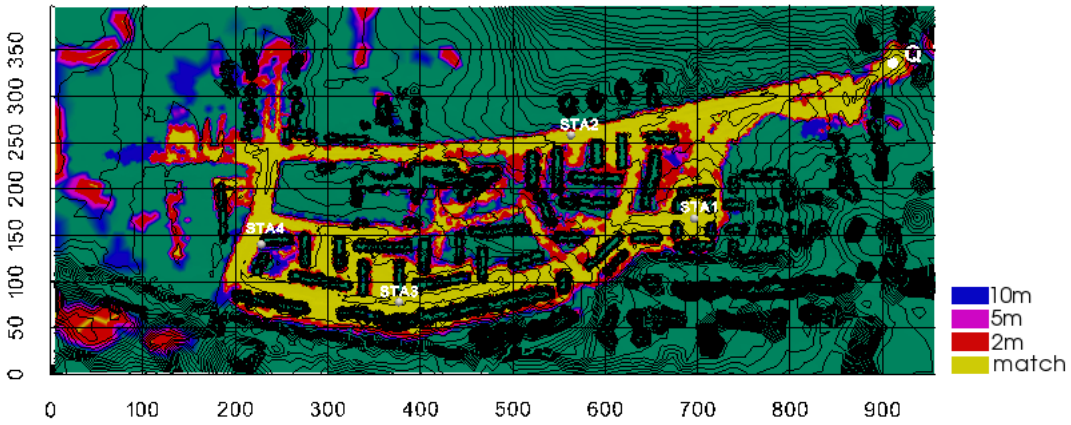

Figure 15: Comparison of maximum flood extent obtained from 3D modelling with different mesh resolutions.

with a high mesh resolution of $2\,m$ is used here. Figure 17 shows the differences in the water depth at $t = 40\,min$ in the computational domain, which is caused by the uncertainty of the inflow discharge. The larger differences of water depth are mainly observed in the southwest region around $STA3$. When the perturbations of $\pm 10\%$ and $\pm 20\%$ are introduced into the inflow discharge (figure 6), the corresponding largest differences in the water depth are $0.17\,m$ and $0.232\,m$ respectively.

Figures 18 and 19 show the time series of the water depth and velocity at locations $STA1 - 4$ simulated with the inflow discharges (figure 6) plus a perturbation of $\pm 10\% \sim \pm 20\%$. It can be seen that as the inflow is reduced, there is a slight lag in the peak time of the water depth and velocity at each location. For example, there is a delay of $1.18\,min$ in the peak of the water depth when a perturbation of -20% is introduced to the inflow discharge (table 2). Table 2 and figure 20 show the sensitivity of the water depth with respect to the inflow discharge. It is observed that the uncertainty from the inflow discharge (perturbation within 20%) mainly affects the flooding peak and ponding processes. For example, a large relative difference of -10.33% in the water depth occurs during the peak period at $STA1$ when a perturbation of -20% is introduced to the inflow discharge. Whereas, an inflow perturbation of $+20\%$ results in differences in water depth, during the ponding period, of 10.03% and 11.56% at locations $STA3$ and $STA4$ respectively.

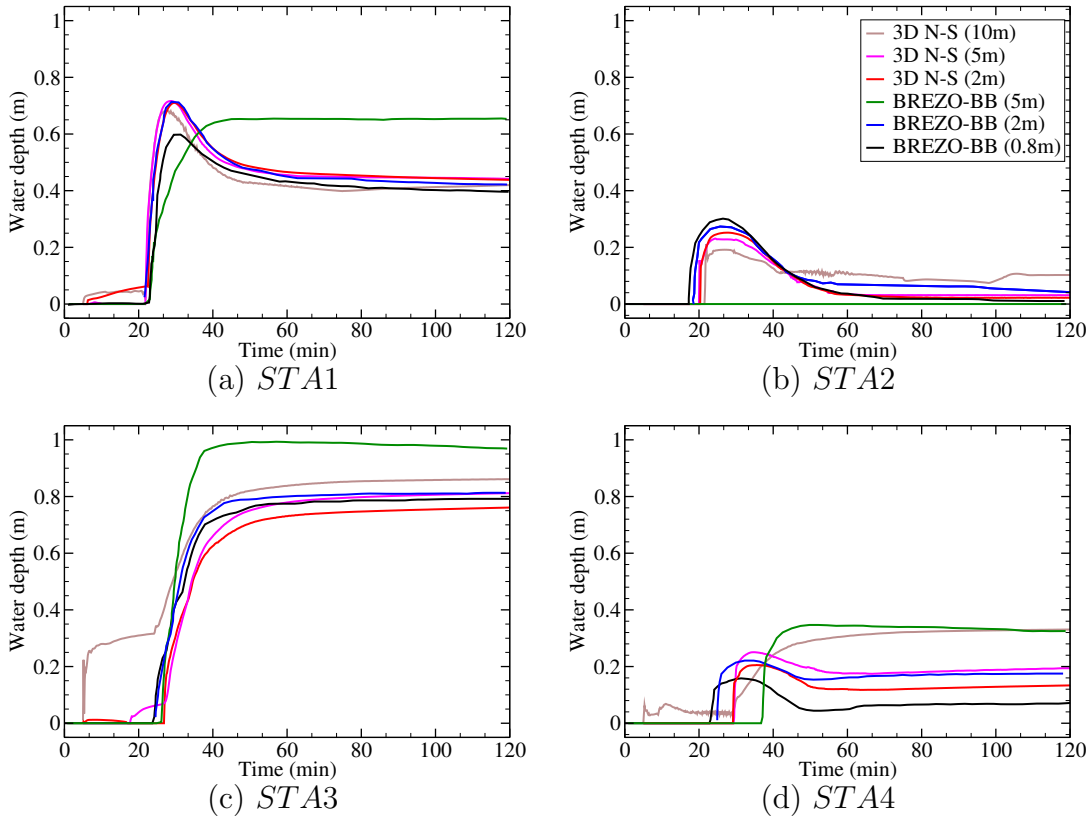

Figure 16: A comparison between the time series of water depth simulated by the 3D N-S model and the published results modelled by the BREZO-BB model[3] at points $STA1-4$ marked on figure 2.

3.6. Comparison of 2D and 3D modelling results at detector locations

Several 2D models are chosen from [2] for the current benchmarking study of the 3D flood model. These 2D hydraulic models include 2D shallow water equations models, such as implicit finite-difference models (TUFLOW [35] and DIVAST [36]), explicit finite-difference model (DIVAST-TVD [37, 38]) and explicit finite-volume model (TRENT [39]) and diffusion equation models, such as explicit finite-difference model (JFLOW [17]) and explicit analytical model (LISFLOOD-FP [19]). For details of these 2D models, see [2]. Schubert *et.al* [3] have compared their 2D modelling results with [2] to assess the sensitivity of urban flood modelling to model formulation for this test site. Here, we choose results of D-TVD, LISFLOOD, TRENT and TUFLOW from [2] to compare with our 3D results. The DIVAST model closely follows

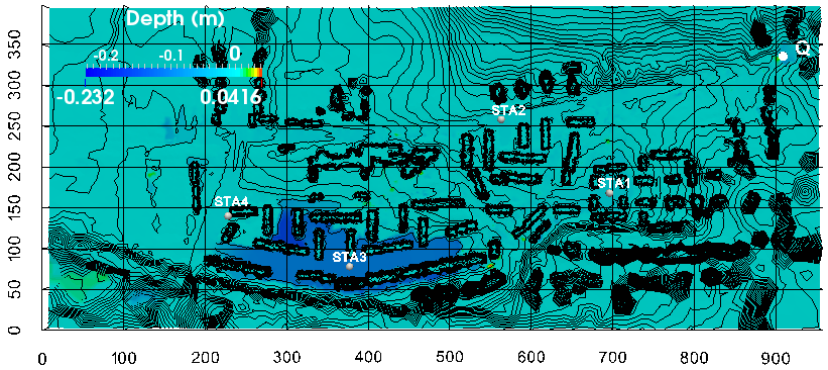

(a) A perturbation of -20% in the inflow discharge

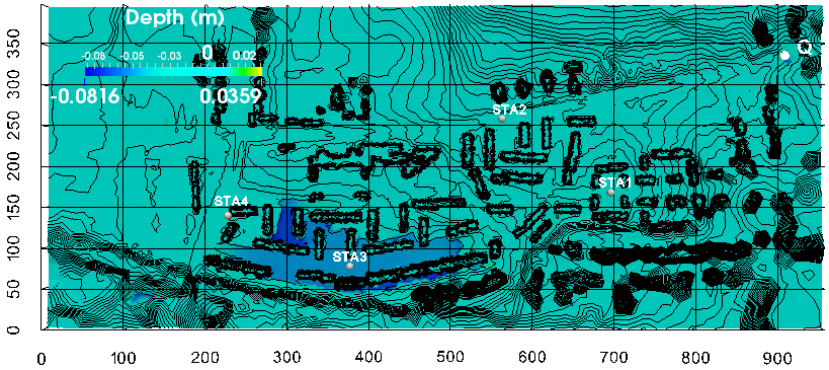

(b) An perturbation of -10% in the inflow discharge

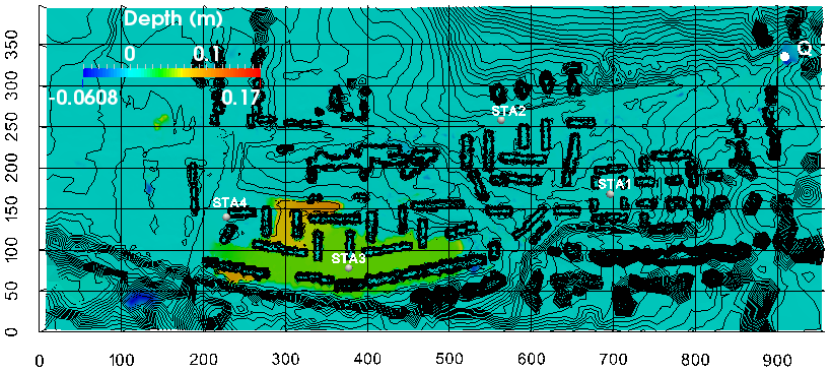

(c) An perturbation of $+10\%$ in the inflow discharge

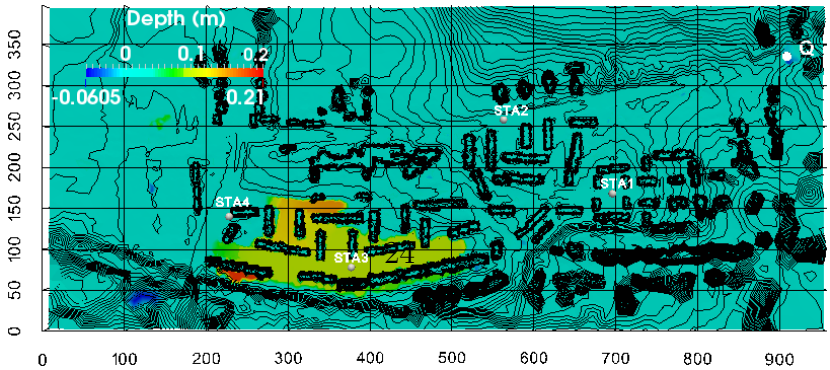

(d) An perturbation of $+20\%$ in the inflow discharge

Figure 17: The differences in water depth at time level $t = 40\,min$ in the computational domain are caused by the uncertainty of the inflow discharge. An perturbation of $\pm 10\% \sim \pm 20\%$ is added into the inflow discharge (figure 6).

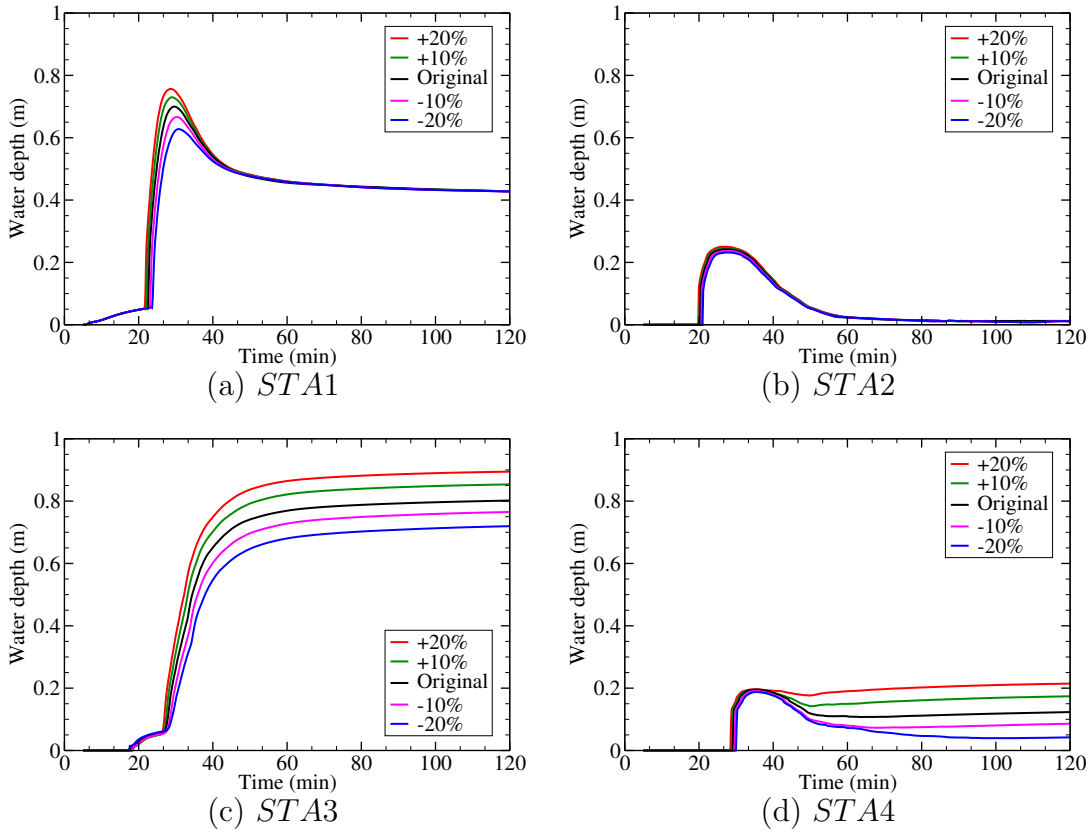

Figure 18: The time series of water depth at detectors, simulated by the 3D N-S model (with a high mesh resolution of $2\,m$) with the inflow boundary condition (see figure 6) without (original) and with a perturbation of $\pm 10\% \sim \pm 20\%$.

the D-TVD prediction, and JFLOW is a simple 2D diffusion wave model and does not show additional characteristics compared with the chosen four 2D models, therefore, they are not selected here.

Comparison of 2D and 3D modelling has been undertaken at locations X1-4 (shown in figure 21, note that $STA2$ is from [3] and X2 is from [2]). These four points represent four different hydraulic situations. Figure 22 shows the time series of water depth predicted by the 3D model and four 2D models, with $2\,m$ mesh resolution. Deep water ponds are observed around X1 and X3 during most of the simulation including the latter parts. A good agreement is observed between 2D and 3D results at locations X1 and X3. Furthermore, all the simulations, including both 3D and 2D, predict similar results at X1 and X3. The reason is that a flat water surface is predicted in ponded areas

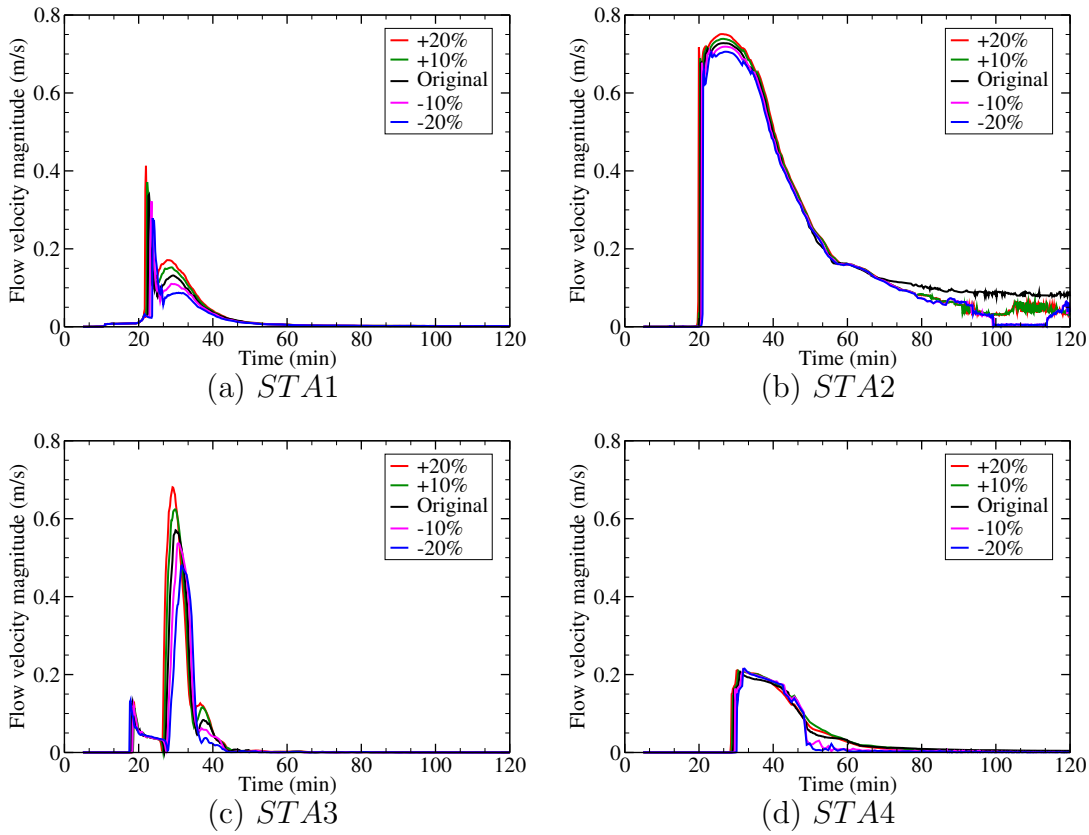

Figure 19: The time series of the flow velocity at detectors, simulated by the 3D N-S model (with a high mesh resolution of $2\,m$) with the inflow boundary condition (see figure 6) without (original) and with a perturbation of $\pm 10\% \sim \pm 20\%$.

regardless of bed elevation [14], and the vertical inertial and non-hydrostatic pressure terms are very small, so the impact of 3D flow structures can be ignored. The differences between 2D and 3D results are, however, relatively large at locations X2 and X4. The reason for this is that both X2 and X4 are on gentle slopes ($< 3\%$) with a relatively high elevation. This elevation prohibits water from ponding there, and makes the vertical inertial and non-hydrostatic pressure terms more important than those areas with more ponding water (X3 and X1, for example).

Here three indicators, including two absolute indicators (mean difference MAE, defined in equation 15, root-mean-square deviation RMSD, see equation 16, also known as root-mean-square error RMSE) and one relative indicator (normalized RMSD, see equation 17), are adopted to assess the difference

Location	-20% inflow	-10% inflow	+10% inflow	+20% inflow
STA1	-10.33%	-4.78%	4.28%	8.07%
STA2	-4.15%	-1.88%	1.73%	3.45%
STA3	-10.25%	-4.58%	6.46%	11.56%
STA4	-3.83%	-1.98%	0.28%	10.03%

Table 2: Sensitivity of the maximum water depth to inflow boundary condition.

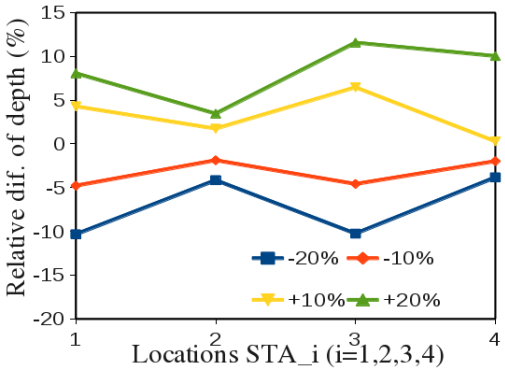

Figure 20: Maximum relative difference represents the sensitivity of the water depth to the inflow boundary condition for the 3D N-S model with a high mesh resolution of $2\,m$.

and similarity between the 3D and 2D modelling results at points X1-4. The mean difference is calculated from the mean absolute error MAE:

$$\mathrm{MAE} = \frac{1}{N}\sum_{n=1}^{N} |\eta_{1,n} - \eta_{2,n}|\,, \tag{15}$$

where, $\eta_{1,n}$ is the water depth at the n^{th} time step obtained from the 3D $2\,m$ simulation, while $\eta_{2,n}$ is the solution of one particular 2D model in [2] (TUFLOW for example) at the same time as $\eta_{1,n}$, and N is the number of time steps. We define the RMSD (D_{rms}) as:

$$D_{rms} = \sqrt{\frac{\sum_{n=1}^{N}(\eta_{1,n} - \eta_{2,n})^2}{N}}, \tag{16}$$

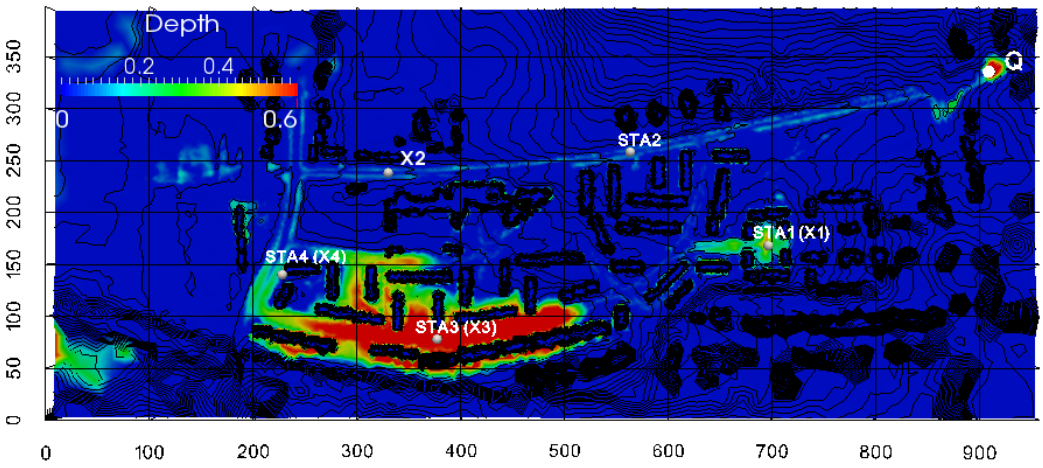

Figure 21: Flood inundation map at the end of the simulation with detectors in [3] ($STA1-4$) and [2] ($X1-4$).

and the normalized RMSD ($\overline{D}_{rms}$) as:

$$\overline{D}_{rms} = \frac{D_{rms}}{\eta_{2,max} - \eta_{2,min}}, \tag{17}$$

where, $\eta_{1,max}$ and $\eta_{1,min}$ are the maximum and minimum 2D solutions over the simulation period. The difference in water depth (MAE) between the 3D $2\,m$ model and the 2D models, is up to $5.27\,cm$ (at X3), which is very close to the maximum difference between the four 2D models which is $5.22\,cm$ (at X3, see table 3). In terms of RMSD, the differences between the 3D and 2D results reach up to $5.86\,cm$ (at X3), which is less than the maximum difference between the 2D models, $6.82\,cm$ (at X3, see table 4). Both the MAE and RMSD between the 3D and 2D results are of the same order of magnitude as that between the different 2D results and the typical random component of LiDAR data vertical error (estimated to be $5\,cm$ RMSD).
Although absolute indicators like the mean difference MAE and RMSD provide detailed quantitative values of the differences between the 3D and 2D results, they are not sufficient to provide a comprehensive assessment. Normalized RMSD (NRMSD, see equation 17) is a good relative indicator that supplements the absolute ones. From table 5, it is observed that the NRMSD values between the 3D and 2D models are much larger at X2, X4 (up to 26.79% and 20.81%, respectively) than that at X1, X3 (less than 7.95%),

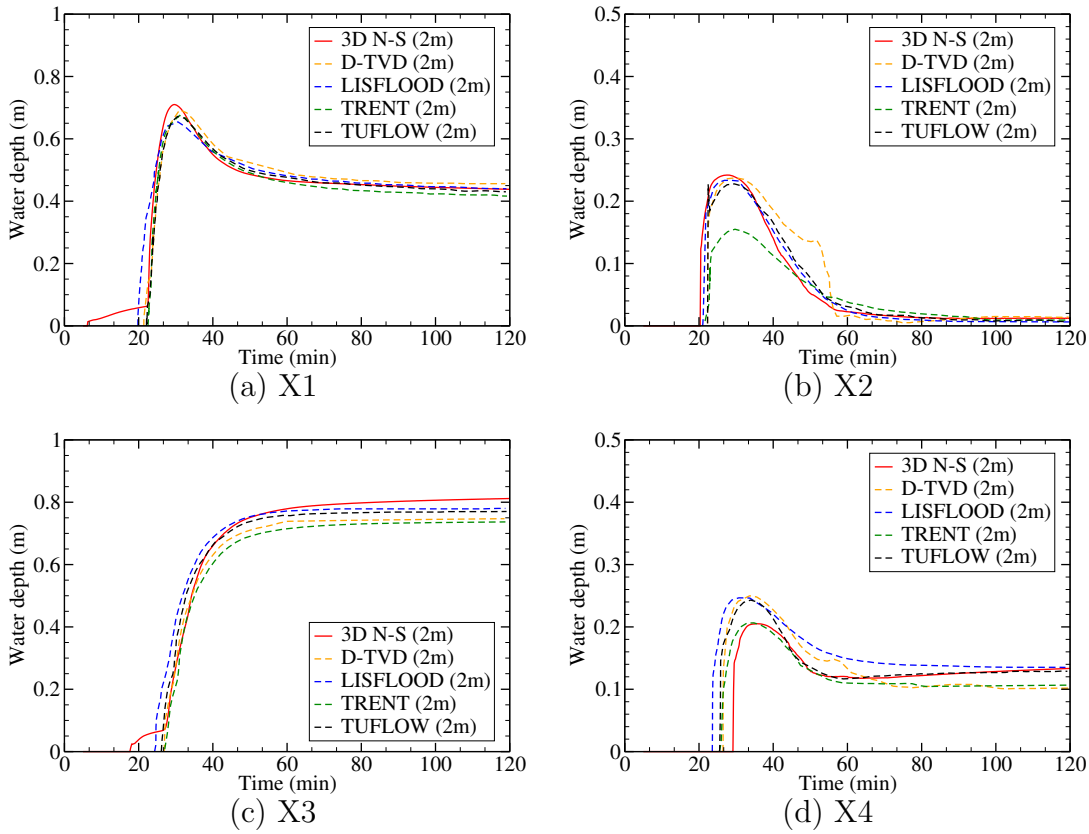

Figure 22: A comparison between the time series of water depth simulated by the 3D N-S model and the published results modelled by other 2D models at points X1-4 (see [2]).

while the NRMSD values between those 2D models are 5.94% at X2 and 18.57% at X4.

Mesh	Location	D-TVD	LISFLOOD	TRENT	TUFLOW	Max 2D
$2\,m$	X1	2.59	1.88	2.11	1.74	2.64
	X2	3.15	3.44	3.45	2.88	2.61
	X3	4.07	2.76	5.27	2.74	5.22
	X4	2.29	2.59	1.47	1.13	3.18

Table 3: Mean difference of the water depth (MAE) between the 3D ($2\,m$) and 2D ($2\,m$) results published in [2] at locations X1-4. Columns 2-5 show the mean absolute difference between the 3D results and four 2D results, while column 6 represents the maximum MAE between the results from those four 2D models, dimension in cm.

Mesh	Location	D-TVD	LISFLOOD	TRENT	TUFLOW	Max 2D
$2\,m$	X1	3.38	3.88	2.96	3.15	5.3
	X2	4.31	4.76	4.07	4.02	4.06
	X3	4.63	4.41	5.86	3.36	6.82
	X4	3.91	5.13	2.77	3.60	4.21

Table 4: RMSD of the water depth between the 3D ($2\,m$) and 2D ($2\,m$) results published in [2] at locations X1-4. Columns 2-5 show the RMSD between the 3D results and four 2D results, while column 6 represents the maximum RMSD between the results from those four 2D models, dimension in cm.

Mesh	Location	D-TVD	LISFLOOD	TRENT	TUFLOW	Max 2D
$2\,m$	X1	4.95	5.92	4.44	4.73	8
	X2	18.34	20.39	26.79	17.69	5.94
	X3	6.20	5.65	7.95	4.37	10.29
	X4	15.77	20.81	13.64	15.03	18.57

Table 5: Normalized RMSE (%) between the water depth series of 3D ($2\,m$) and the 2D ($2\,m$) results published in [2] at locations X1-4. Columns 2-5 show the mean absolute difference between the 3D results and four 2D results, while column 6 represents the maximum NRMSD between the results from those four 2D models.

Figure 23 depicts the data in table 3 - 5 and provides a more intuitive representation of the differences in terms of the three indicators. It can be observed

that the 3D modelling results match TUFLOW better than all the other 2D models in general. The reason may be that TUFLOW is an implicit full 2D shallow water equations model, which is closest to the proposed fully-implicit 3D Navier-Stokes equation model. Both the absolute and relative indicators show that the differences between the 3D and each 2D model are mainly identical (the points cluster together within a narrow range) at X1. This is likely because X1 is a flat area with buildings surrounding it (see figure 2) which makes it a relatively closed space, providing good ponding conditions. The absolute and relative indicators present very different patterns of the differences between the 3D and 2D results at locations X2 and X3. Although at X3 the absolute differences between the 3D and each 2D model (the value at X3 in figure 23(a) and (b)) are large and also vary largely (the points scatter in a wide span at X3 in figure 23(a) and (b)), the relative indicator NRMSD is very small due to the large absolute water depth. With smaller water depth, X2 and X4 presents more appreciable differences (higher value in comparison with both the 3D-2D results and intra-2D results) in terms of NRMSE. Despite the characteristics analyzed above, the 3D $2\,m$ model generally stays within the ensemble spread of the 2D models except at X2, where all the indicators of differences between the 3D and 2D models are beyond the maximum values within those 2D models. According to [14], that may be due to the fact that the hydrostatic and diffusive-wave approximations are not appropriate as slope (and velocity) increases.

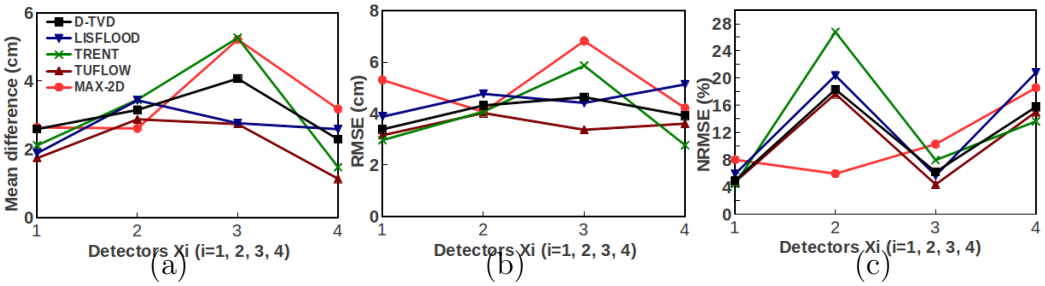

Figure 23: The mean difference (MAE), RMSD and NRMSD represent the difference between the results simulated by the 3D N-S model and some popular 2D models in [2] with $2\,m$ mesh resolution at points X1-4.

4. Conclusions and future work

Recently, a new 3D unstructured full N-S urban flooding model has been developed in [1]. In the current paper, this 3D urban flooding model has been applied to a $1.0\,km \times 0.4\,km$ urban catchment within the perimeter of the city of Glasgow.

Very detailed information has been provided by the 3D simulation, including the spatial variation of vertical velocity. Local flow details can be seen clearly and directly in enlarged 3D section views. The results have shown good agreement with the published results of several 2D shallow water equations models [2] in terms of flooding maps and water depth in ponded areas. Large velocities (including vertical velocities) can be observed in areas with denser topographic contours which denote steeper slopes. Also, appreciable vertical velocities have been observed around buildings and other objects.

Sensitivity of the 3D unstructured model to mesh resolution has been studied with three different meshes. Upon comparison of the inundation extent with the 2D BREZO-BB model results in [3], the 3D model presents different sensitivity and specificity to mesh resolution. With coarse unstructured meshes, the 3D model performs much better than the 2D BREZO-BB model.

In comparison with four 2D models from [2], the 3D results generally match the results of 2D models very well in ponded regions (X1 and X3), because a flat water surface is predicted in these areas regardless of bed elevation [14]. Also, the vertical inertia and non-hydrostatic feature are very small, therefore, the impact of 3D flow structures can be ignored. However, relatively larger differences between the 3D and 2D results can be observed in areas with greater terrain gradient and shallower water depth (X2 and X4). This is likely because the vertical inertial and non-hydrostatic pressure terms become more important as the terrain gradient increases.

This is a first attempt at applying a 3D unstructured mesh flooding model to a real urban flood, and satisfactory results have been obtained. Currently, the main difficulty in the application of this method to larger spacial scales is due to the computational burden. There are two ways to save computational time, further optimization of algorithm and parallel computing. Our future work in urban flood modelling will focus on the following aspects: (1) integrated modelling of surface runoff (3D) and underground pipe network flow (1D); (2) improvement of computational efficiency; (3) physical forces of the floodwaters which act on buildings; (4) integrated modelling of the 3D hydrodynamic model and risk assessment models.

Acknowledgments

This work was carried out under funding from the UK's Natural Environment Research Council (project NE/J015938/1), the Engineering and Physical Sciences Research Council (EP/I00405X/1), the EU Natural Hazards consortium grant, and with support from the the Imperial College Appllied Modelling and Computational Group (AMCG), High Performance Computing Service and the Grantham Institute for Climate Change. Ting Zhang would like to acknowledge the support from China Scholarship Council and the assistance of Saba Manzoor, PhD student at Imperial College London, and Dr. A. Avdis. Prof I.M. Navon acknowledges the support of NSF ATM grant.

References

[1] T. Zhang, F. Fang, C.C. Pain, A. Avdis, Č. Maksimović, P. Feng, I.M. Navon, A. Candy. A three-dimensional unstructured-mesh flooding model using a new wetting and drying method in a high aspect ratio domain. Technical report, Imperial College London.

[2] Hunter N.M. and Bates P.D., et al. Benchmarking 2D hydraulic models for urban flooding. Proceedings of the ICE-Water Management, 2008; 161(1):13–30.

[3] Schubert, Jochen E. and Sanders, Brett F. and Smith, Martin J. and Wright, Nigel G. Unstructured mesh generation and landcover-based resistance for hydrodynamic modelling of urban flooding. Advances in Water Resources, 2008; 31(12):1603–1621.

[4] G.E. Hollis. The effect of urbanization on floods of different recurrence interval. Water Resources Research, 1975; 11(3):431–435.

[5] A.H. Elliott, S.A. Trowsdale. A review of models for low impact urban stormwater drainage. Environmental Modelling & Software, 2007; 22: 394–405.

[6] Leopold, L.B. Hydrology for urban land planning: A guidebook on the hydrologic effects of urban land use. Washington D.C., 1968.

[7] N. Nirupama, and Slobodan P. Simmonovic. Increase of flood risk due to urbanisation:A Canadian example. Natural Hazards, 2007; 40: 25–41.

[8] Julien Lhomme. Large-scale urban floods modelling and two-dimensional shallow water models. 7th International Conference on Hydroinformatics HIC, 2006; Nice, France:1–8.

[9] Zerger, A., Smith, D.I., Hunter, G.J., Jones, S.D. Riding the storm: A comparison of uncertainty modelling techniques for storm surge risk management. Applied Geography, 2002; 22: 307–330.

[10] Christopher Zoppou. Review of urban storm water models. Environmental Modelling & Software, 2001; 16: 195–231.

[11] S.W. funke, C.C. Pain, S.C. Kramer, M.D. Piggott. A wetting and drying algorithm with a combined pressure/free-surface formulation for non-hydrostatic models. Advances in Water Resources, 2011; 34: 1483–1495.

[12] Wang Xin, Zhixian Cao, Gareth Pender and Guangming Tan. Modelling of urban flooding due to Yangtze River dike break. Proceedings of the ICE-Water Management, 2011; 164(1):3–14.

[13] Humberto A. Gallegos, Jochen E. Schubert, Brett F. Sanders. Two-dimensional, high-resolution modelling of urban dam-break flooding: A case study of Baldwin Hills, California. Advances in Water Resources, 2009; 32: 1323–1335.

[14] T.J. Fewtrell, P.D. Bates, M. Horritt and N.M. Hunter. Evaluating the effect of scale in flood inundation modelling in urban environments. Hydrol. Process., 2008; 22: 5107–5118.

[15] Jian Chen , Arleen A. Hill, Lensyl D. Urbano A GIS-based model for urban flood inundation Journal of Hydrology, 2009; 373: 184–192.

[16] Hilary K. McMillan, James Brasington. Reduced complexity strategies for modelling urban floodplain inundation. Geomorphology, 2007; 90: 226–243.

[17] Bradbrook K.F., Lane S.N., Waller S.G., Bates P.D. Two dimensional diffusion wave modelling of flood inundation using a simplified channel representation. International Journal of River Basin Management, 2004; 2(3): 211–223.

[18] Werner M., Blazkova S., Petr J. Spatially distributed observations in constraining inundation modelling uncertainties. Hydrol. Process., 2005; 19(16): 3081–3096.

[19] Hunter N.M., Horritt M.S., Bates P.D., Wilson M.D. and Werner M.G. An adaptive time step solution for raster-based storage cell modelling of floodplain inundation. Advances in Water Resources, 2005; 28(9), 975–991.

[20] James D. Brown, Tom Spencer and Iris Moeller. Modelling storm surge flooding of an urban area with particular reference to modelling uncertainties: A case study of Canvey Island, United Kingdom. Water Resources Research, 2007; 43(6).

[21] Qiuhua Liang, Guozhi Du, Jim W. Hall, and Alistair G.L. Borthwick. Flood inundation modelling with an adaptive quadtree grid shallow water equation solver. J. Hydraul. Eng., 2008; 134: 1603–1610.

[22] Neil M. Hunter, Paul D. Bates, Matthew S. Horritt, Matthew D. Wilson. Simple spatially-distributed models for predicting flood inundation: A review. Geomorphology, 2007; 90: 208–225.

[23] Lindsey Ann LaRocque, Mohamed Elkholy, M. Hanif Chaudhry and Jasim Imran. Experiments on urban flooding caused by a levee breach. J. Hydraul. Eng., 2013; 139: 960–973.

[24] S.N. Lane, K.F. Bradbrook, K.S. Richards, P.A. Biron, A.G. Roy. The application of computational fluid dynamics to natural river channels: three-dimensional versus two-dimensional approaches. Geomorphology, 1999; 29: 1–20.

[25] Djordjević, Slobodan and Saul, Adrian J., et al. Experimental and numerical investigation of interactions between above and below ground drainage systems. Water Science & Technology, 2013; 67(3).

[26] Galambos, Istvan. Improved understanding of performance of local controls linking the above and below ground components of urban flood flows. PhD thesis, University of Exete, 2012.

[27] Yu, D., Lane, S.N. Urban fluvial flood modelling using a two-dimensional diffusion-wave treatment. Part 1: mesh resolution effects. Hydrological Processes, 2006; 20(7): 1541–1565.

[28] Geuzaine, Christophe, and JeanFranois Remacle. Gmsh: A three-dimensional finite element mesh generator with built-in pre- and post-processing facilities. Journal for Numerical Methods in Engineering, 2009; 79(11): 1309-1331.

[29] Pain C.C., Piggott M.D., Goddard A.J.H., Fang F., et al. Three-dimensional unstructured mesh ocean modelling. Ocean Modelling, 2005; 10(1): 5–33.

[30] R.G. Lerner, G.L. Trigg. Encyclopaedia of Physics (2nd Edition), 1991.

[31] G. Freni, G. La Loggia and V. Notaro. Uncertainty in urban flood damage assessment due to urban drainage modelling and depth-damage curve estimation. Publisher: Water Science & Engineering, 2010.

[32] Meyer V. & Messner F. Flood damage, vulnerability and risk perceptionchallenges for flood damage research. Book series NATO Science Series: IV: Earth and Environmental Sciences, 67, Netherlands, 2006. (Online).

[33] Smith, D.I. Flood damage estimation- A review of urban stage-damage curves and loss functions. Water S. A., 1994; 20(3): 231-238.

[34] Begnudelli L., Sanders B.F., Bradford S.F. An adaptive Godunov-based model for flood simulation. J Hydraul Eng, 2008; 134(6): 714725.

[35] Syme W.J. Dynamically Linked Two-dimensional/One-dimensional Hydrodynamic Modelling Program for Rivers. Estuaries & Coastal Waters, MEngSc thesis, University of Queensland, Australia, 1991.

[36] Falconer R.A. A water quality simulation study of a natural harbor. American Society of Civil Engineers, Journal of Waterway, Port, Coastal and Ocean Engineering, 1986; 112(1): 15–34.

[37] Liang D., Falconer R.A. and Lin B. Comparison between TVD-MacCormack and ADI-type solvers of the shallow water equations. Advances in Water Resources, 2006; 29(12): 1833–1845.

[38] Liang D., Lin B. and Falconer R.A. Simulation of rapidly varying flow using an efficient TVD-MacCormack scheme. International Journal for Numerical Methods in Fluids, 2007; 53(5): 811–826.

[39] Villanueva I. and Wright N.G. Linking Riemann and storage cell models for flood prediction. Proceedings of the ICE-Water Management, 2006; 159(1): 27–33.

[40] Gomes-Pereira L.M., Wicherson R.J. Suitability of laser data for deriving geographical data: a case study in the context of management of fluvial zones. ISPRS Journal of Photogrammetry and Remote Sensing, 1999; 54(23): 105–114.

[41] Cobby D.M., Mason D.C. and Davenport I.J. Image processing of airborne scanning laser altimetry for improved river flood modelling. ISPRS Journal of Photogrammetry and Remote Sensing, 2001; 56(2): 121–138.

[42] Hedstrom G.W. and Osterheld A. The effect of cell Reynolds number on the computation of a boundary layer. Journal of Computational Physics, 1980; 37: 399–421.